Lab on a Chip

PAPER

View Article Online
View Journal | View Issue

Check for updates

Cite this: *Lab Chip*, 2025, **25**, 3467

Engineering neuronal networks in granular microgels to innervate bioprinted cancer organoids on-a-chip†

Jacob P. Fredrikson, [abcd] Daniela M. Roth,[abcd] Jameson A. Cosgrove,[abd] Gulsu Sener,[bd] Lily A. Crow,[abd] Kazumi Eckenstein,[d] Lillian Wu,[abd] Mahshid Hosseini, [abde] George Thomas,[df] Sebnem Ece Eksi[bdg] and Luiz Bertassoni *[abcdeg]

Organoid models are invaluable for studying organ processes *in vitro*, offering an unprecedented ability to replicate organ function. Despite recent advancements that have increased their cellular complexity, organoids generally lack key specialized cell types, such as neurons, limiting their ability to fully model organ function and dysfunction. Innervating organoids remains a significant challenge due to the asynchronous biological cues governing neural and organ development. Here, we present a versatile organ-on-a-chip platform designed to innervate organoids across diverse tissue types. Our strategy enables the development of innervated granular hydrogel tissue constructs, followed by the sequential addition of organoids. The microfluidic device features an open tissue chamber, which can be easily manipulated using standard pipetting or advanced bioprinting techniques. Engineered to accommodate microgels of any material larger than 50 μm, the chamber provides flexibility for constructing customizable hydrogel environments. Organoids and other particles can be precisely introduced into the device at any stage using aspiration-assisted bioprinting. To validate this platform, we demonstrate the successful growth of primary mouse superior cervical ganglia (mSCG) neurons and the platform's effectiveness in innervating prostate cancer spheroids and patient-derived renal cell carcinoma organoids. This platform offers a robust and adaptable tool for generating complex innervated organoids, paving the way for more accurate *in vitro* models of organ development, function, and disease.

Received 7th February 2025,
Accepted 11th April 2025

DOI: 10.1039/d5lc00134j

rsc.li/loc

Published on 15 aprile 2025. Downloaded on 06/02/2026 22:13:02.

Introduction

Neural innervation plays a pivotal role in development, function, and homeostasis across biological systems.[1–6] Through sensory input, direct intercellular communication, and paracrine signalling, the nervous system orchestrates critical processes that regulate tissue dynamics and response to environmental cues. Most *in vitro* models used to study organogenesis and disease states lack intrinsic innervation,[5,7,8] limiting the study of biological processes and diseases where innervation is particularly important, as in many cancers where innervation influences tumour initiation, progression, and metastasis.[9–13]

Organoid models are invaluable for studying normal and diseased organ processes *in vitro*, offering unparalleled replication of organ function.[14–18] These complex, heterogeneous cell structures derived from stem cells have been developed for most organs and are widely utilized in studies ranging from disease modelling to drug development.[18,19] Despite recent advancements that have increased their cellular complexity, most organoids still lack key specialized cell types, such as neurons, limiting their ability to fully represent organ function and dysfunction.[16,20] A select few have successfully generated innervated cochlear and pancreatic organoids, which were shown to more accurately represent their *in situ* counterparts.[6,21,22] However, most organoid subtypes remain nerve-free.[14,20] Therefore,

[a] *Knight Cancer Precision Biofabrication Hub, Knight Cancer Institute, Oregon Health and Science University, Portland, OR 97201, USA.*
E-mail: bertasso@ohsu.edu
[b] *Cancer Early Detection Advanced Research Center (CEDAR), Knight Cancer Institute, Oregon Health and Science University, Portland, OR 97201, USA*
[c] *Department of Oral Rehabilitation and Biosciences, School of Dentistry, Oregon Health and Science University, Portland, OR 97201, USA*
[d] *Knight Cancer Institute, Oregon Health and Science University, Portland, OR 97201, USA*
[e] *Department of Biomedical Engineering, School of Medicine, Oregon Health and Science University, Portland, OR 97201, USA*
[f] *Department of Pathology and Laboratory Medicine, Oregon Health and Science University, Portland, OR, 97201, USA*
[g] *Division of Oncological Sciences, Knight Cancer Institute, Oregon Health and Science University, Portland, OR, 97201, USA*

† Electronic supplementary information (ESI) available. See DOI: **https://doi.org/10.1039/d5lc00134j**

Published on 15 aprile 2025. Downloaded on 06/02/2026 22:13:02.

there remains a need to develop organoid/spheroid neural engineering strategies that are applicable to a broad range of tissue types, and enable more reliable models of organ development, function, and disease.

One key challenge to enabling the engineering of innervated tissue constructs, including organoids and spheroids, is the asynchronous biological cues governing organoid development and neural growth.[14] Ideally, engineering strategies should enable the formation of mature and stable interconnected neuronal networks that can fully innervate the tissue of interest. This is complicated by the fact that neural cells often undergo network formation and maturation at a different rate and under different culture conditions from the desired organoids, making engineering of innervated organoids particularly challenging.

Here, we present a versatile organ-on-a-chip platform designed to innervate organoids and spheroids across various tissue types. Our strategy relies on the utilization of a microfluidic device featuring an open tissue chamber that can be freely manipulated from the top using standard pipetting or nozzle-based bioprinting techniques. The open tissue chamber is populated with a neural cell-laden jammed granular hydrogel, which can be cultured under optimized neuronal growth conditions for as long as needed prior to organoid loading, allowing for neuronal network formation and stabilization over time. The self-healing nature of the jammed granular hydrogels pre-populated with neuronal networks allows spheroids or organoids of any kind to be robotically dispensed at pre-determined locations in three-dimensions, thus addressing the long-standing challenge of facilitating neuronal innervation of any kind of organoid/spheroid for tissue engineering applications. To validate this platform, we demonstrate the successful growth of primary mouse superior cervical ganglia (mSCG) neurons and the platform's effectiveness in innervating prostate cancer spheroids and patient-derived renal cell carcinoma organoids. This platform represents a promising tool for creating complex innervated organoids, bypassing the need for more complicated genetic or biofabrication methods.

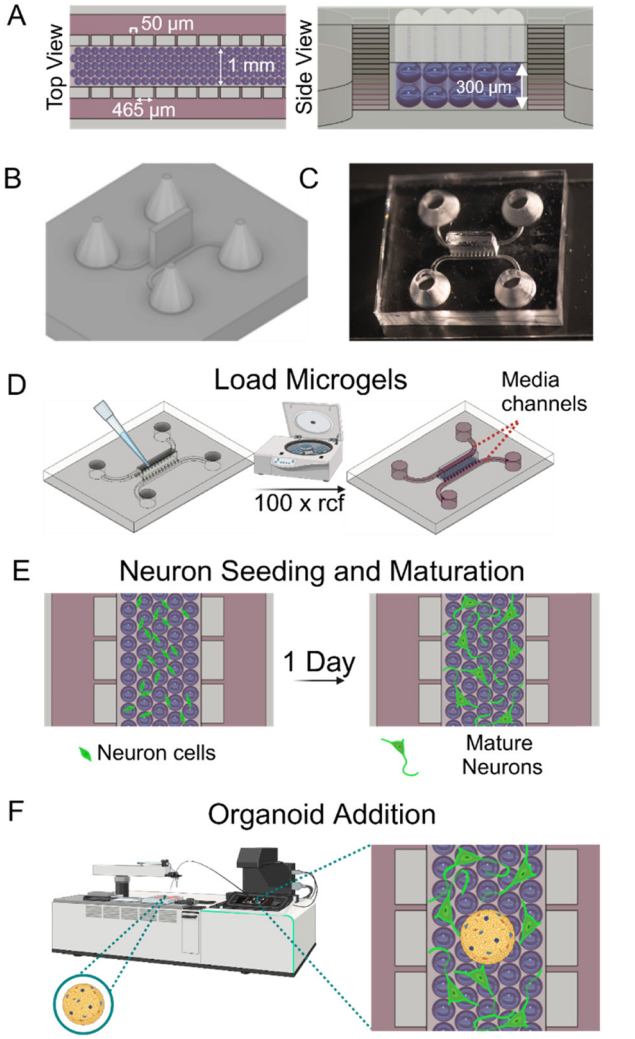

Fig. 1 Device design and schematics. (A) Schematic of top and side views of the device loaded with microgels. (B) CAD drawing of the negative master-mold. (C) Photograph of the device. (D–F) Schematic of how microgels are loaded into the device, neurons are cultured, and organoids are added to the device.

Results and discussion

Device design and experimental workflow

To build a platform capable of innervating a broad range of organoids, we developed a microfluidic device with a pre-innervated granular hydrogel that is open to a nozzle-based bioprinting technique. The device has a central tissue chamber that confines packed microgels and is open on top. The central tissue chamber measures 1 × 5.7 mm. Additionally, there are two lateral channels for media exchange (Fig. 1A). Between the lateral and central channels are rectangular pillars with gaps of 50 μm. This width is sufficiently large to allow cell migration between pillars but small enough that microgels >50 μm would be unable to pass through. The two side channels are enclosed on top and bottom with two ports for media exchange (Fig. 1A). The central tissue chamber follows a similar design to a device from Krattiger *et al.*; however, it is open on top, such that it is manipulable with a pipette or many nozzle-based bioprinting techniques.[23] The combination of these three techniques, namely the granular microgel fabrication, open top microfluidics, and organoid/spheroid bioprinting, is what makes our approach unique.

Of the many methodologies for building microfluidic devices, we chose to use soft lithography due to the small device features needed to immobilize microgels. Typical photolithography approaches have maximum *z*-features of less than 400 μm, making it challenging to create high depth tissue chambers that are more friendly to organoid placement/bioprinting. Multi-layered devices require complicated fabrication techniques and are often inaccurate. To increase the accessibility of the device, we sought to make a single-layer device that still meets all

 This journal is © The Royal Society of Chemistry 2025

our design criteria. We thus chose to use digital light processing (DLP) printing to fabricate our negative master mold (Fig. 1B). The mold design is such that the resulting polydimethylsiloxane (PDMS) slabs do not need to be modified and can be immediately bonded to glass slides or coverslips.

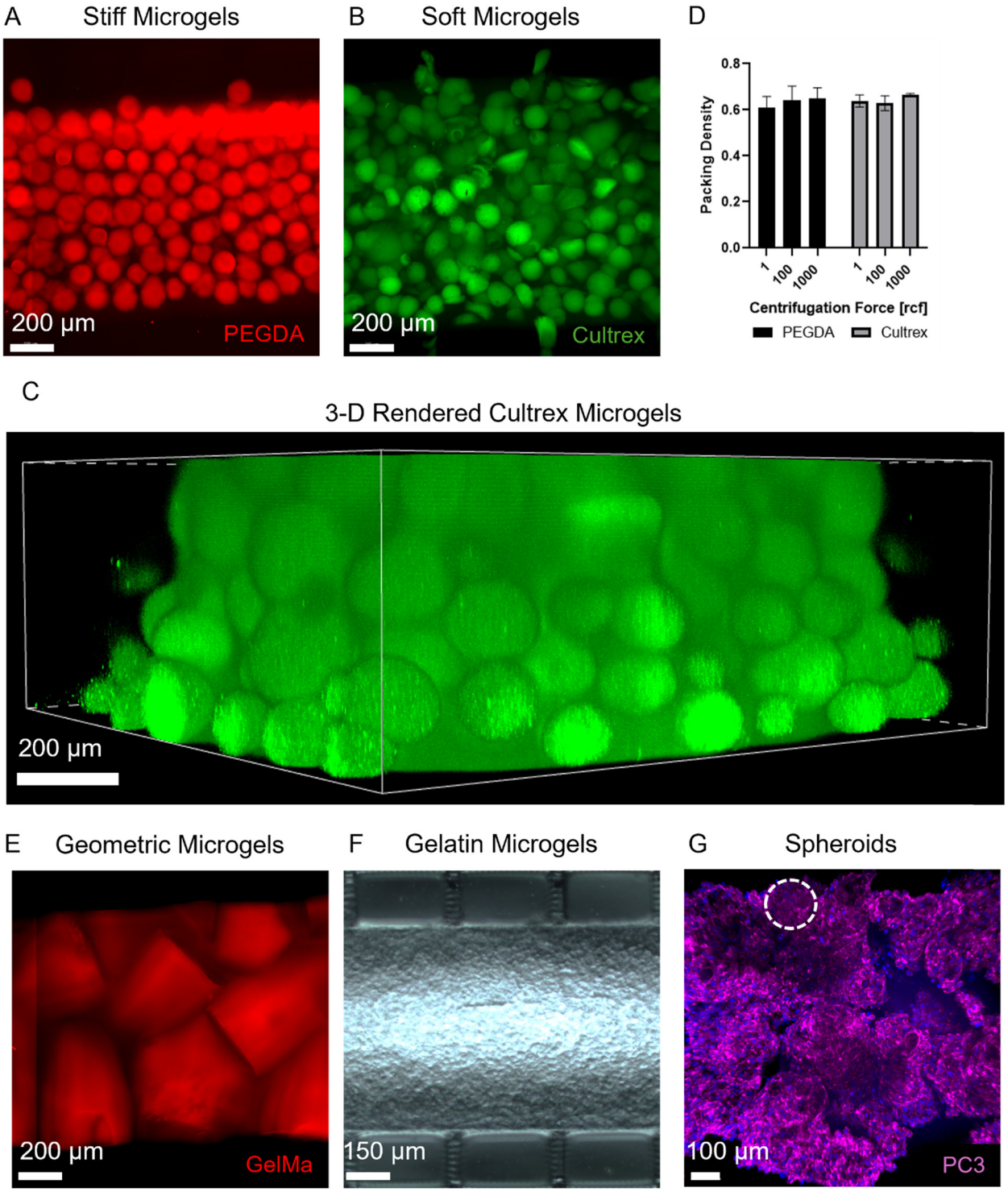

Fig. 2 Microgel confinement on chip. (A) A granular PEGDA hydrogel on chip. (B) A granular Cultrex hydrogel on chip. (C) A 3-D rendering of a granular Cultrex hydrogel on chip. (D) Graph of microgel packing density for PEGDA and Cultrex microgels as a function of centrifugation force. Microgels were added *via* pipette and allowed to settle under gravity (1 rcf) or were centrifuged at 100 or 1000 rcf for 20 seconds. No value was significantly different from the theoretical packing density of randomly jammed rigid spheres. (E) A granular hydrogel on chip comprised of 3-D printed GelMA microgels. (F) A granular gelatin hydrogel similar to those used in FRESH printing. (G) A structure of packed PC3 spheroids. The dotted circle is the approximate outline of a single spheroid.

Published on 15 aprile 2025. Downloaded on 06/02/2026 22:13:02.

Published on 15 aprile 2025. Downloaded on 06/02/2026 22:13:02.

To increase device accessibility and reproducibility, we sought to make the operation of the device as simple as possible. The microgels and other materials can be added to the central tissue chamber with simple pipetting and centrifugation (Fig. 1C and D). Cells can be seeded simultaneously with microgels or at later time points and allowed to mature. Cells can additionally be added to the lateral channels for infiltration/migration studies. For more complex studies, the central tissue chamber is open to bioprinting techniques such as aspiration-assisted bioprinting (Fig. 1C). In our study, we seeded dissociated neurons simultaneously with microgels, allowed them to mature, and then added spheroids and organoids with aspiration-assisted bioprinting (Fig. 1E and F). However, the workflow is flexible and can be adjusted to best accommodate various experimental goals.

Microgel confinement on-chip

Granular hydrogels offer several advantages over their monolithic counterparts, such as enhanced cell mobility, improved nutrient diffusion, and self-healing properties. These features make them an ideal choice for our objective of adding organoids to a pre-innervated hydrogel. We first sought to demonstrate the range of microgels the device was capable of confining. We fabricated 150 μm, 10 wt% polyethylene glycol diacrylate (PEGDA) microgels using standard drop-based microfluidics techniques. Microgels were concentrated in microcentrifuge tubes and added to the device with a pipette (Fig. 1D). The device demonstrated excellent immobilization of the PEGDA microgels with minimal escape of microgels from the tissue chamber (Fig. 2A). At a concentration of 10 wt%, PEGDA typically has an elastic modulus in the order of 10 kPa, which is considered relatively stiff.[24] We would expect the microgels to minimally deform and thus be easily trapped by the pillars present in the device. However, PEGDA and other stiff hydrogel materials are suboptimal for neuron growth. To investigate how the device would immobilize comparatively soft microgels, we fabricated 150 μm Cultrex microgels using drop-based microfluidics and loaded them onto the device with a pipette.[25] Cultrex, a Matrigel alternative, has an elastic modulus in the order of 100 Pa, making it well suited for neuron growth.[26] However, its low stiffness also makes it highly deformable under pressure. Using enclosed devices, the pressures needed to flow a jammed solution of Cultrex microgels into a tissue chamber would deform the microgel and allow them to pass through the barriers of the tissue chamber.[23] Here, by loading the devices from the top with just a pipette, we found that the device contained Cultrex microgels with minimal numbers of microgels escaping into the side channels (Fig. 2B). We found that the Cultrex microgels formed dense three-dimensional (3-D) structures of microgels typically ranging from 200–400 μm in height (Fig. 2C). The height of the microgel bed can be easily adjusted by varying the amount of microgels added to the chamber. The ability to make granular hydrogels from soft microgels on-a-chip greatly expands the range of tissues that can be grown on the chip.

We then compared how different centrifugation forces would affect the packing density of the PEGDA and Cultrex microgels. Microgels were added to the tissue chamber with a pipette and then allowed to settle by gravity or were centrifuged at 100–1000 × g for 20 seconds. We found that centrifugation did not significantly alter the overall packing density in either hydrogel type (p = 0.35) (Fig. 2D, ESI† Fig. S1A). Interestingly, we found that Cultrex microgels deformed slightly when centrifuged at 1000 × g, but this did not noticeably affect the packing density (Fig. 2D, ESI† Fig. S1B). A randomly jammed structure of equal-diameter rigid spheres typically has a packing density of 63.5%.[27,28] In all tested conditions, the packing densities did not significantly deviate from this value ($p > 0.46$). To prevent cells from potentially adhering to the upper walls of the device, we used centrifugation forces of 100 × g for all later experiments.

While we tailored the device to accommodate soft microgels such as Cultrex, the device can immobilize an extensive range of microparticles to build custom granular materials. Uniform-hexagonally packed spheres have a theoretical packing limit of ~74%; however, in some cases, it may be desirable to achieve greater packing densities.[28] The jamming of nonuniform spheres can achieve significantly higher theoretical packing densities compared to uniform spheres.[28] Therefore, we aimed to demonstrate that the device was capable of containing nonuniform particles as well. We generated polydisperse PEGDA microgels using batch emulsion methods and loaded them onto the device using a pipette.[29–31] The device was effective at containing the microgels, but some microgels with diameters <50 μm escaped through the gaps in the pillars (ESI† Fig. S2).

Additionally, many studies have demonstrated that extracellular matrix (ECM) geometry influences cell differentiation and migration.[32,33] To explore this further, we aimed to demonstrate the device's ability to contain nonspherical microgels. Star-shaped Gelatin methacryloyl (GelMA) microgels were 3-D printed using DLP printing and resolved as elongated stars. Geometric microgels were designed to be 400 μm across and 300 μm tall, too large to be injected into typical microfluidic devices. However, since our tissue chamber is open to pipetting, we could easily inject the large microgels (Fig. 2E). These large particles further demonstrate the range of microgels that the device supports. Particles that were previously uninjectable due to size or mechanical constraints can be simply placed into the tissue chamber.

Many advanced bioprinting techniques, such as Freeform Reversible Embedding of Suspended Hydrogels (FRESH) and sacrificial writing into functional tissue (SWIFT) bioprinting, use granular materials as support materials for printing complex 3-D structures.[34–36] To further demonstrate the device's applications, we added granular materials similar to those used in FRESH and SWIFT bioprinting. The device

 This journal is © The Royal Society of Chemistry 2025

Published on 15 aprile 2025. Downloaded on 06/02/2026 22:13:02.

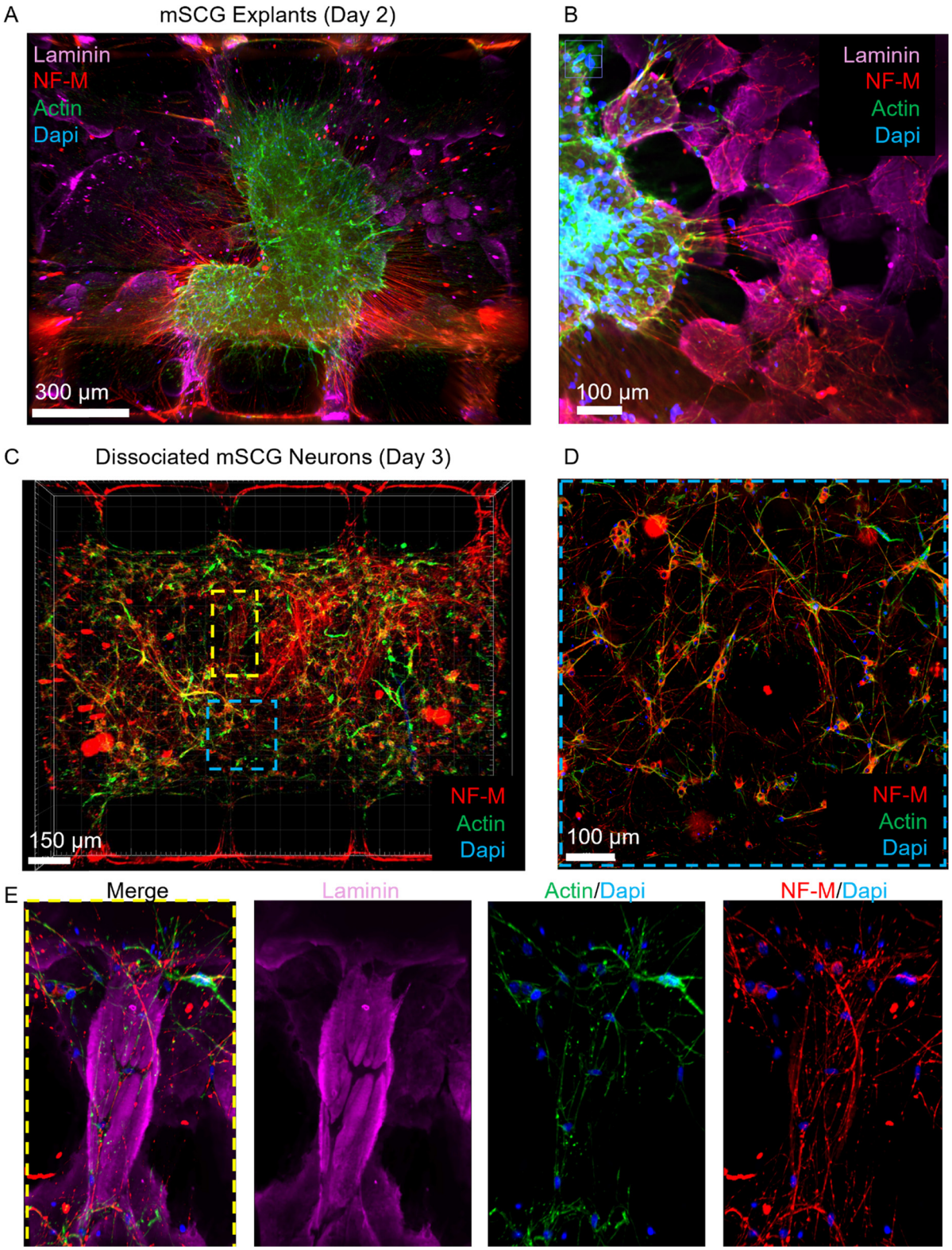

Fig. 3 Development of a pre-innervated granular hydrogel construct on-a-chip. (A) mSCG explants were added to the granular Cultrex hydrogel. Explants were allowed to grow for 2 days prior to fixation. Samples were stained for nuclei (Hoechst), actin, neurofilament-H, and laminin (Cultrex microgels). The image is a maximum *Z*-projection. (B) A single *z*-slice of the mSCG explants. (C) Dissociated mSCG neurons were cultured in a granular Cultrex hydrogel for 3 days prior to fixation. Samples were stained for nuclei, actin, and NF-H. The image is a maximum *Z*-projection. (D) A single *z*-slice of the dissociated mSCG neurons. (E) A zoomed image of mSCG reorganizing their local ECM and aligning axons to form early nerve bundles.

Published on 15 aprile 2025. Downloaded on 06/02/2026 22:13:02.

effectively immobilized the gelatin microgels used in FRESH bioprinting (Fig. 2F) and packed spheroids like those used in SWIFT bioprinting (Fig. 2G).

The open tissue chamber presented in this platform significantly broadens the range of granular hydrogels that can be effectively integrated on-chip. The device can accommodate microgels with diverse elastic moduli, shapes, and sizes, offering unparalleled flexibility for customizing ECM environments tailored to specific experimental needs. Many tissues, such as the brain and other organs, require softer ECM materials for proper development. Using this device, hydrogels such as Cultrex, Matrigel, collagen, and hyaluronic acid, could all be developed as granular hydrogels on-chip to better mimic a range of native ECMs.

Development of a pre-innervated granular hydrogel on chip

Next, we used the Cultrex microgels to develop a pre-innervated granular hydrogel construct. Previous work has shown that granular hydrogels are an excellent substrate for neuron growth *in vitro* and *in vivo*.[37–39] Primary neurons can be cultured *in vitro* using two main approaches: explant culture, where ganglia are dissected and directly cultured on a dish, or dissociated culture, where ganglia are dissociated into individual neurons prior to culture. We sought to demonstrate that this device can grow neurons in either form. Using aspiration-assisted bioprinting, we added mSCG ganglia to the tissue chamber loaded with packed Cultrex microgels. Explants were allowed to grow for two days prior to fixation. After two days, explants had grown throughout the entire chip and expressed neurofilament-medium (NF-M), a neuronal maturation marker (Fig. 3A). NF-M-positive axons were seen growing onto, across, and into the Cultrex microgels, which were visualized using laminin antibodies, a main component of Cultrex. These findings indicated that the granular Cultrex hydrogel provided a supportive growth environment for the mSCG neurons (Fig. 3A and B). Interestingly, the neurons significantly remodelled the Cultrex (ESI† Fig. S3A and B). Small Cultrex bridges were observed where neurons grew between microgels, and gaps in the Cultrex were visible, indicating neuronal remodelling of the local ECM. Interestingly, actin staining was concentrated within the explant, while NF-M staining was primarily localized in the extending axons (Fig. 3B). 3-D renderings and *z*-stacks showed that the explant grew radially in 3-D, extending not only along the bottom of the device but also throughout the packed microgels (Fig. 3A, ESI† Movie S1).

Explants are excellent options for specific studies and offer valuable localized insights, though they may introduce heterogeneity across the entire device. Next, we wanted to develop a homogeneous innervated granular hydrogel construct from dissociated neurons. Dissociated SCG neurons were mixed with Cultrex microgels at 2×10^6 cells per mL and loaded onto the device. The cells were allowed to grow for three days and were then fixed. After three days, neurons grew throughout the entire granular tissue construct (Fig. 3C, ESI† Movie S2). Neurons expressed NF-M throughout their axons and soma (Fig. 3D). In many regions, neurites could be seen following the curvature of the granular hydrogel (Fig. 3D), and neurons located within the granular hydrogel had different morphologies compared to those on the bottom of the device (Fig. 3D, ESI† Fig. S4). As in our explant experiments, we found localized regions of the structure where the neurons had heavily remodelled the ECM (Fig. 3E, ESI† Fig. S3C). In these regions, we found that the neurons had reorganized the matrix and oriented their axons parallel to one another, suggesting that the neurons were beginning to form nerve bundles (Fig. 3E). Additionally, in these regions, the neurites displayed a high abundance of NF-M and minimal actin expression, suggesting greater neuronal maturation.

In summary, we demonstrate two different methodologies for forming innervated granular hydrogel tissue construct on-a-chip. The platform supports the growth of either SCG explants or dissociated SCGs, providing a high level of flexibility for designing further experiments. The granular hydrogel constructs provided an excellent growth environment, yielding mature neurons in three days or less.

Innervation of prostate cancer spheroids

Growing evidence suggests that neurosignaling plays a significant role in altering cancer progression, metastasis, and therapy resistance.[40–43] However, despite evidence that the intercellular signalling between neurons and cancer is essential to cancer progression, the mechanisms of nerve recruitment into the tumour microenvironment (TME) are poorly understood due to the lack of relevant *in vitro* models.[3,41] Likewise, the influence of neuronal innervation on the proliferation of cancer cells across different cancer types remains poorly understood. We thus sought to build a universal platform that can be used to innervate cancer spheroids and organoids. Prostate cancer is one of the highly innervated tumour types where nerve density is highly correlated with high-grade tumour progression.[3,44] Therefore, we first demonstrated the platform's potential for innervating spheroids using prostate cancer cells. Spheroids were generated by encapsulating PC3s, an established prostate cancer cell line at a concentration of 1×10^7 cells per mL in Cultrex microgels using batch emulsion methodology and preculturing spheroids in growth medium for 3 days. Meanwhile, mSCG neurons were dissociated and mixed with Cultrex microgels. The microgels and neurons were loaded into the device with a pipette and grown on-chip for 1 day. Next, a robotic cell/spheroid dispenser (Sartorius CellCelector) was used to select spheroids between 200–300 μm in diameter and add the chosen spheroids to the pre-innervated chip. The spheroids and neurons were cocultured for 2 days prior to fixation. PC3 spheroids were stained for CD31 (a PC3 marker) to distinguish PC3 from neuronal cells and define the boundary of the spheroid.[45] mSCG neurons

 This journal is © The Royal Society of Chemistry 2025

Published on 15 aprile 2025. Downloaded on 06/02/2026 22:13:02.

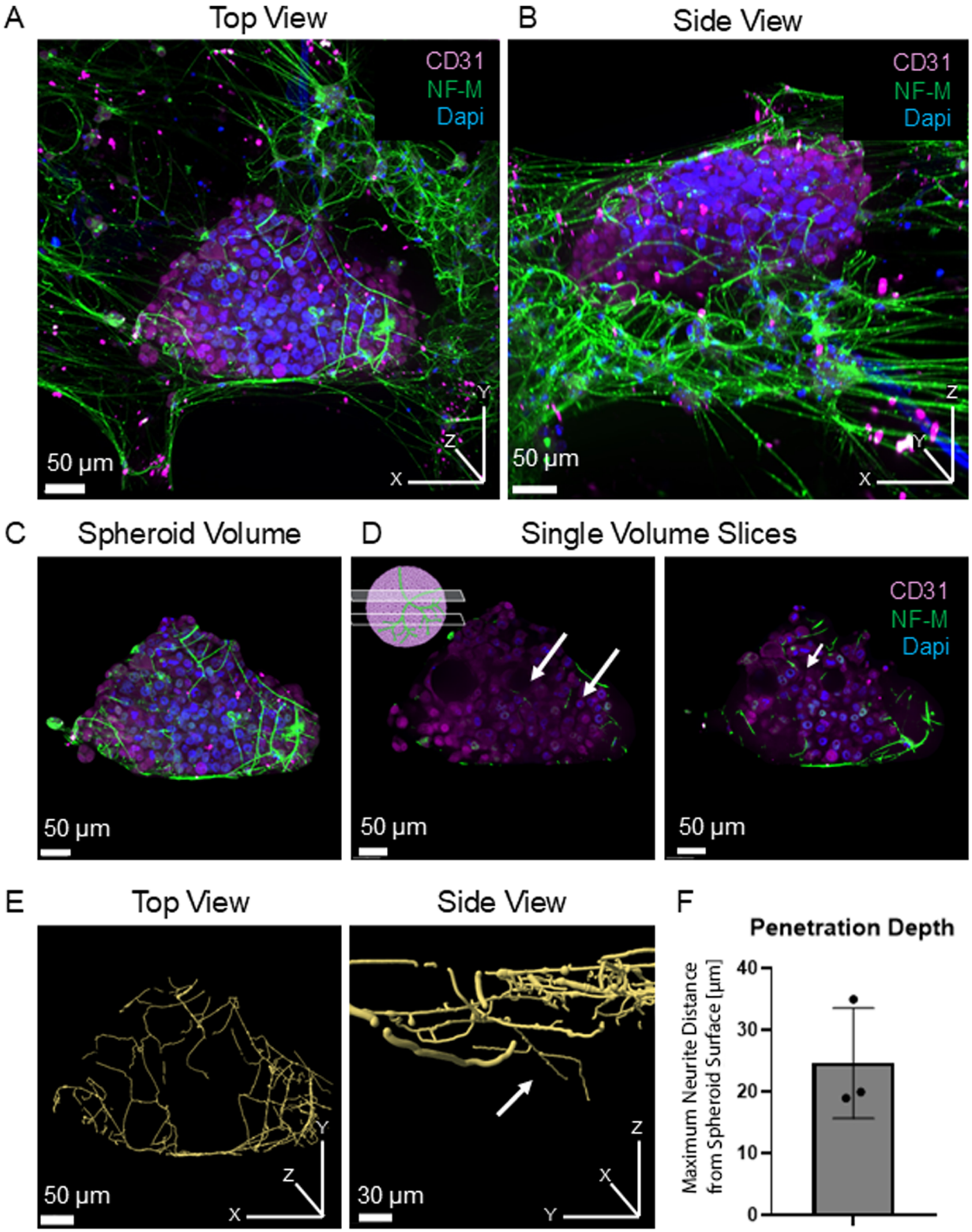

Fig. 4 Innervation of prostate cancer spheroids. Dissociated mSCG neurons were cultured in granular Cultrex hydrogels for 1 day. Subsequently, PC3 spheroids were placed into the granular hydrogel using aspiration-assisted bioprinting and cultured for 2 days prior to fixation. Samples were stained for nuclei (Hoechst), CD31 (to distinguish PC3 cells), and NF-H (axons). (A) A *z*-projection of an innervated PC3 spheroid. (B) The same spheroid rotated to show depth. (C) Surface tools in Imaris were used to render the spheroid volume and exclude staining outside of the spheroid. (D) Single *z*-slices of the spheroid volume showing the penetration depth of the axons (white arrows). (E) Filaments tools in Imaris were used to trace neurites within the spheroid. Images are *Z*-projections from the top and side views. (F) Graph of the penetration depth of axons into PC3 spheroids. Measurements were the furthest an axon was from the edge of the spheroid.

Published on 15 aprile 2025. Downloaded on 06/02/2026 22:13:02.

were stained for neurofilament-H to distinguish neurons from PC3 cells and to visualize axon location. After only 3 days of coculture, PC3 spheroids appeared embedded within the pre-innervated beds and had recruited NF-M positive axons to the spheroids (Fig. 4A, ESI† Fig. S5A and B). This result signifies a major step forward for innervated tumour models. Spheroids and neurons were allowed to develop separately, benefitting the independent growth and maturation of an interconnected neurite network into which spheroids could be placed directly into with additional support from the granular hydrogels (Fig. 4B). We saw no obvious adverse effects on the neurons, and microgels remained stable surrounding the spheroids after their addition (ESI† Fig. S6).

To look at only neurons directly interacting with the PC3 spheroids, Imaris image processing software's surface tools were used to exclude NF-M signal not colocalized within the spheroid (Fig. 4C, ESI† Fig. S5A and B). NF-M positive axons were found along the surface and throughout the interior of the spheroids (Fig. 4D, white arrows, ESI† Movie S3). Imaris filament tools were used to trace only axons within the spheroids (Fig. 4E, ESI† Fig. S5A and B). Spheroids contained total axon lengths of 572 ± 238 μm (ESI† Fig. S5C). Axons were found to have achieved maximum penetration depths of 25 ± 9 μm into the spheroids (Fig. 4F), indicating that the neurons were not only on the surface but were well within the boundary of the spheroids.

Innervation of renal cell carcinoma organoids

While many cancers such as prostate, pancreatic ductal adenocarcinoma (PDAC), and head and neck are highly innervated cancers, neurons likely still play a role in less innervated cancers.[46] To further demonstrate the potential for the platform to innervate a variety of tumour models, including cell-line derived spheroids and primary, patient-derived tumour organoids, we cocultured patient-isolated renal cell carcinoma (RCC) organoids with mSCG neurons. Research on the role of the nervous system in RCC is limited, likely due to the lack of relevant *in vitro* models. To address this gap, we aimed to build a model capable of studying these interactions. To begin, RCC organoids were cultured in Matrigel domes following supplier protocols. Mature RCC organoids were mixed with dissociated mSCG neurons and

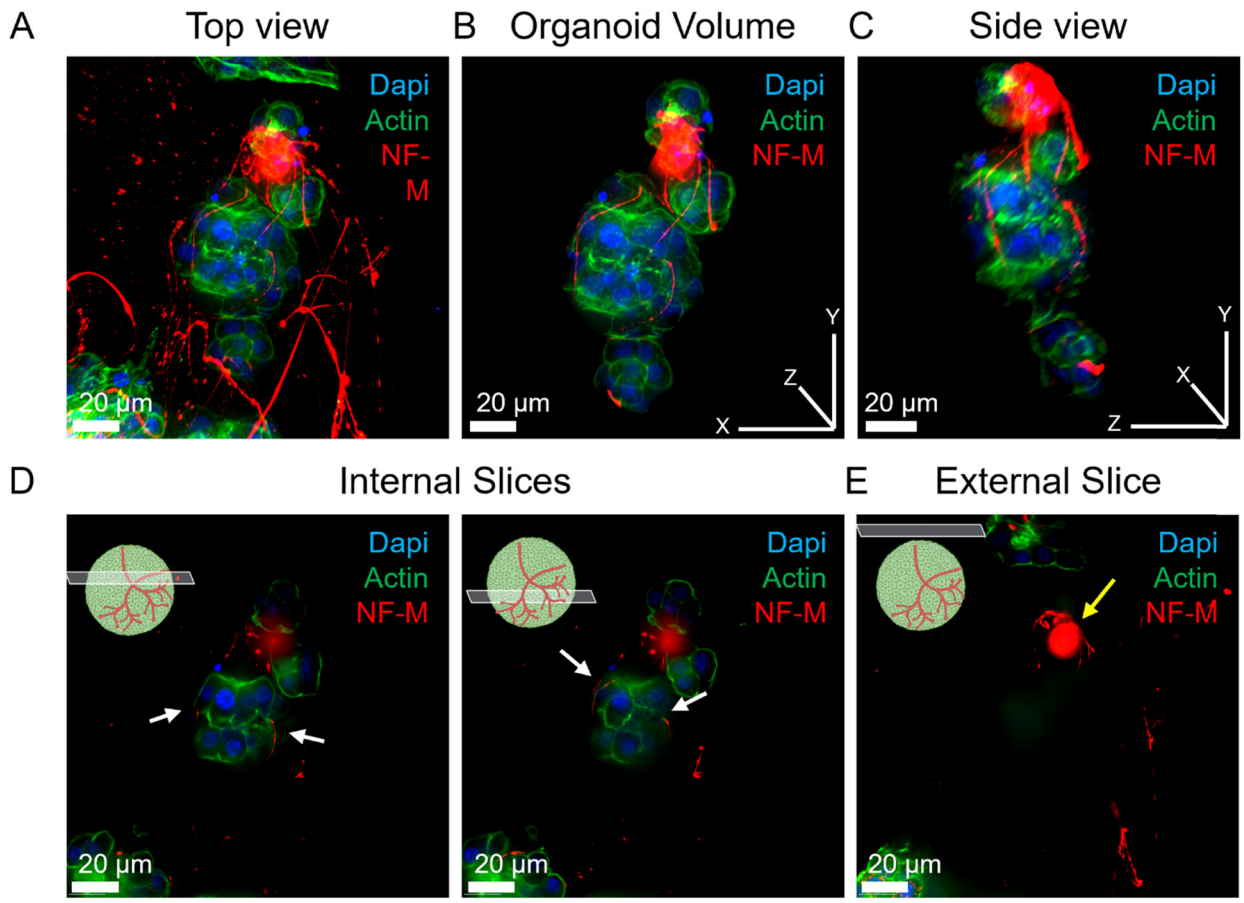

Fig. 5 Innervation of renal cell carcinoma organoids. Dissociated mSCG neurons and RCC organoids were cultured in a granular Cultrex hydrogel for 4 days prior to fixation. Samples were stained for nuclei (Hoechst), actin, and NF-H (axons). (A) A *z*-projection of an innervated RCC organoid. (B) Surface tools in Imaris were used to render the organoid volume and exclude staining outside of the organoid. (C) The same organoid rotated to show depth. (D) Single *z*-slices of the organoid volume showing the penetration of the axons (white arrows). (E) Single *z*-slices of the organoid volume showing a neuron soma external to the organoid (yellow arrow).

 This journal is © The Royal Society of Chemistry 2025

Published on 15 aprile 2025. Downloaded on 06/02/2026 22:13:02.

Cultrex microgels and loaded into the device with a pipette. RCC organoids and mSCG neurons were cocultured for 4 days before fixation. After 4 days of coculture, RCC organoids were surrounded by NF-M-positive axons and had recruited axons into the organoids (Fig. 5A). To focus exclusively on neurons directly interacting with the RCC organoids, Imaris image processing surface tools were used to exclude NF-M signals not colocalized within the organoids (Fig. 5B). Neurons were observed surrounding the organoids (Fig. 5A and B) and penetrating toward their centers (Fig. 5D, white arrows, ESI† Movie S5). Interestingly, neuronal somas were frequently located near the organoids but remained external to them (Fig. 5E, yellow arrow).

Next, we investigated how neurons affected RCC organoid growth and development. We compared KI67 expression, a marker of cell proliferation, in RCC organoids cocultured with mSCG neurons to RCC organoids cultured without neurons. High levels of KI67 could be detected in both conditions but with significantly more expression in innervated samples (Fig. 6A). Organoids that were cocultured with mSCG neurons expressed KI67 in 52 ± 20% of cells/organoid, a significantly higher fraction of cells compared to organoids that were cultured without neurons, 24 ± 19% ($p <$ 0.0001) (Fig. 6B). Interestingly, there was at least one KI67-positive cell in all the organoids analyzed that were cocultured with neurons (Fig. 6A and B). In contrast, approximately 22% of the organoids cultured without neurons did not express KI67 (Fig. 6A and B). Additionally, the number of cells in each organoid nearly doubled when organoids were cocultured with neurons compared to those cultured without (with neurons: 29 ± 25 cells/organoid, without neurons: 15 ± 12 cells/organoid, $p = 0.0176$) (Fig. 6C). These combined results demonstrate that nerves increased the proliferation of cancer cells in innervated RCC organoids.

As cancers progress from preneoplastic lesions to tumours, nerves are recruited from the surrounding tissues into the tumour microenvironment.[3,41,43,44] These nerves, in turn, stimulate angiogenesis and proliferation of the cancer cells while preventing cell death and modulating immune response.[3,44,46,47] Here, we demonstrated how our platform can be used to study how innervation influences cancer proliferation, a crucial step toward developing novel cancer therapeutics. These effects likely arise from paracrine signaling and the release of proliferation-increasing neurotransmitters; however, additional studies are necessary to evaluate the responsible molecular mechanisms. While we

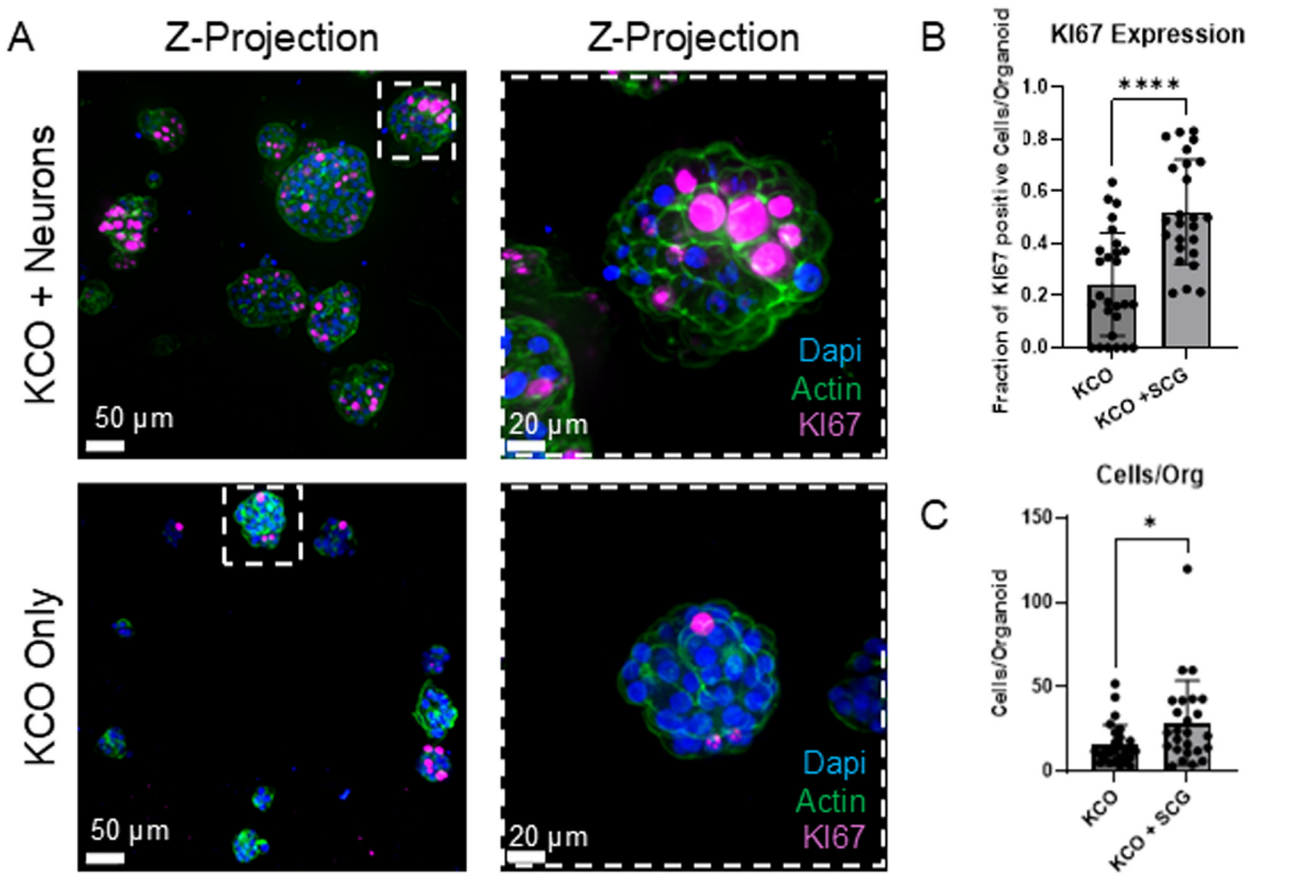

Fig. 6 Innervation increases RCC organoid proliferation. Dissociated mSCG neurons and RCC organoids were cultured in a granular Cultrex hydrogel for 4 days prior to fixation. Samples were stained for nuclei (Hoechst), actin, and KI67. (A) Representative images of RCC organoids cultured with or without neurons including an inset of a single organoid. (B) Comparison of KI67 expression in organoids cultured with or without neurons. Each dot represents one organoid. Data is presented as the fraction of cells in each organoid that expresses KI67. $p < 0.0001$. (C) Comparison of the number of cells in organoids cultured with or without neurons. Each dot represents one organoid. $p = 0.0176$.

Published on 15 aprile 2025. Downloaded on 06/02/2026 22:13:02.

demonstrate the effects nerves have on cancer, in future work, this system could be used to investigate how cancer induces innervation. This system has the capacity to add cells at different stages of development, is compatible with live-cell imaging, and is 3-D, all critical components of a model to study various types of intercell communication.

Sample removal and histology

One of the strengths of this device is that its open top allows for user interventions after initial loading. Unlike most microfluidic systems that are fully enclosed or require device disassembly to access tissue compartments, our platform enables straightforward sample extraction for downstream analyses. We demonstrated this utility by extracting samples from the device for histological and other downstream processing. After filling the open-top chamber with agarose *via* pipette, we were able to easily remove the entire chamber contents as a single block, which could then be treated as a conventional tissue sample. This sample was compatible with multiple processing methods, including cryosectioning, formalin-fixed paraffin-embedded (FFPE) embedding, immunofluorescence, and histochemical staining. For example, we successfully prepared and characterized organoid (ESI† Fig. S7) and mSCG explant cultures (ESI† fig. S8) after on-chip analyses. The extracted organoids and explants retained their structural integrity and morphological features post-processing. Notably, axonal projections from the mSCG explants were clearly visible, extending from the main explant core, mirroring observations made through on-chip immunofluorescence (ESI† Fig. S8).

Experimental

Microfluidic device fabrication

Microfluidic drop makers. Negative master molds were prepared using standard photolithography techniques.[48,49] Negative master molds were made with SU-8-2100 photoresist on 4″ silicon wafers. The drop makers were prepared to be 150 μm tall. Two-component Sylgard 184 PDMS was mixed at a 10 : 1 ratio by mass, poured over wafers, and degassed. The devices were baked at 60 °C for at least 4 h. The cured devices were cut from the master and ports were punched using a 0.75 mm ID biopsy punch. The devices were plasma-bonded to 3 × 2 in glass slides by exposing the PDMS and glass to oxygen plasma. The bonded devices were baked at 60 °C for at least 1 h to increase the strength of the bond.

Open-top devices. Negative master molds were 3-D printed on a CADworks3D, Series Ultra, Microfluidic Edition 3-D printer using the company's MasterMold for PDMS resin. Masters were cleaned with ethanol and cured under UV light for 60 minutes. CAD files can be found in the supplemental information. Two-component Sylgard 184 PDMS was mixed at a 10 : 1 ratio by mass, poured over wafers, and degassed. The devices were baked at 60 °C for at least 4 h. The cured devices were cut from the master. The devices were plasma-bonded to PDMS-coated glass slides by exposing the slide and PDMS device to corona treatment for 5 seconds. The bonded devices were baked at 60 °C for at least 1 h to increase the strength of the bond and then autoclaved to sterilize the devices.

Microgel production

Monodisperse Cultrex microgels. Cultrex microgels were produced through drop-based microfluidics using previously established protocols.[25,50] Liquid Cultrex Reduced Growth Factor Basement Membrane Extract, Type 2, at 4 °C and 1.5% w/w fluorosurfactant (008, RAN Biotechnologies, MA, US) in HFE7500 (RAN Biotechnologies) were loaded into syringes and injected into a 150 μm drop-maker using syringe pumps in a 4 °C room. The flow rates used were Q_{Cultrex} = 300 μL h^{-1} and Q_{HFE7500} = 1200 μL h^{-1}. All equipment and reagents were refrigerated at 4 °C to prevent premature gelation of the Cultrex. Drops were collected in microcentrifuge tubes and incubated at 37 °C for 60 min to gel the drops. Microgels were stored in HFE7500 until use. The resulting microgels were washed with equal volumes of 1*H*,1*H*,2*H*,2*H*-perfluorooctanal (PFO) – HFE7500 (20% v/v) and phosphate-buffered saline (PBS) to drops. The washed microgels were then collected in PBS. For experiments using fluorescent microgels, 1.2 MDa FITC Dextran was mixed with the liquid Cultrex at a concentration of 0.1% w/v.

Monodisperse PEGDA microgels. PEGDA microgels were fabricated as above, except Cultrex was substituted for 10% w/w PEGDA + 0.1% w/v lithium phenyl-2,4,6-trimethylbenzoylphosphinate (LAP) in PBS, and dropmaking was carried out at room temperature. PEGDA drops were crosslinked by exposure to 405 nm light for 5 minutes. PEGDA microgels were washed as above. For experiments using fluorescent microgels, methacrylated rhodamine was mixed with the PEGDA precursor solution at concentrations of 0.05% w/v.

Polydisperse microgels. Polydisperse PEGDA microgels were produced using batch emulsion methodology by vortexing 10% w/w PEGDA + 0.1% w/v LAP + PBS and 1.5% w/w fluorosurfactant in HFE 7500 at a 1 : 2 ratio for 3 seconds.[31,48,49] PEGDA drops were crosslinked by exposure to 405 nm light for 2 minutes. PEGDA microgels were washed as above.

3D printed GelMA microgels. Geometrically controlled GelMA microgels were fabricated *via* DLP 3D printing on a Bionova X 3D Bioprinter (Cellink, BICO). Microgels were printed according to a computer-aided design of five-point stars, 400 μm across × 300 μm tall, at 90% light intensity and 0.001 mm s^{-1} print speed. A CAD drawing of the print design and an image of a microgel is included in ESI† Fig. S9. The bioink was prepared with 20% w/v GelMA and 0.35% w/v LAP photoinitiator in PBS. The bioink was supplemented with 0.05% w/v methacrylated rhodamine for microgel visualization. The solution was left to dissolve at 60 °C for 10 min, and the temperature was maintained at 37 °C until printing. Post printing, unpolymerized bioink was removed

 This journal is © The Royal Society of Chemistry 2025

Published on 15 aprile 2025. Downloaded on 06/02/2026 22:13:02.

and the resulting microgels were washed with warm PBS. Microgels were removed from the print plate and collected in a microcentrifuge tube. They were then stored in PBS until further use.

Gelatin microgels. Gelatin microgels were purchased from Advanced Biomatrix (#5244). Particles had average diameter of 15–50 μm, were sourced from bovine, and were hydrated following manufacturer protocols.

Cell culture

PC3 cells were cultured in Roswell Park Memorial Institute (RPMI) 1640 Medium supplemented with 10% fetal bovine serum (FBS) + 1% penicillin/streptomycin. Cell media was changed every other day and cells were passaged when they reached 80–90% confluency. All cells were incubated at 37 °C with 5% CO_2 and relative humidity.

Spheroid formation

PC3 spheroids were formed using a batch emulsion method.[31,51,52] PC3 cells were suspended in Cultrex at a concentration of 1×10^7 PC3 cells per mL. Cell-laden Cultrex was mixed at a 1 : 2 ratio with 1.5% w/w fluorosurfactant in HFE 7500 in a 1.5 mL microcentrifuge tube and vortexed for 3 seconds. The resulting emulsion was incubated at 37 °C for 60 min to gel the drops and then washed as the microfluidic Cultrex drops above were. 50 μL of PC3 spheroids were added to a single well of a six-well plate and cultured for 3 days in RPMI 1640 Medium supplemented with 10% FBS + 1% penicillin/streptomycin.

Organoid culture

The organoids (743489-274-T-V1-organoid) used in this study were developed by NCI PDMR. **https://pdmr.cancer.gov/**. Organoids were embedded in ice-cold Cultrex Reduced Growth Factor Basement Membrane Extract (BME), Type 2 (R&D Systems, cat# 3533-010-02) and plated in sterile 24-well plates (Corning, cat# 3526), then incubated for 15 minutes at 37 °C to allow for BME polymerization. After polymerization, NCI media 6A was added, as specified by PDMR SOP30101, consisting of Organoid Basic Media and L-WRN conditioned media at a 1 : 1 ratio and supplemented with 1.25 mM *N*-acetylcysteine (Sigma, cat# A9165), 10 mM nicotinamide (Sigma, cat# 72340), B-27 supplement (Thermo Fisher, cat# 17504044), N-2 supplement (Thermo Fisher, cat# 175002001), and 10 uM Y-27632 (Cayman Chemicals, cat# 10005583); Organoid Basic Media consisted of Advanced DMEM-F12 (Thermo Fisher, cat# 12634028), 100 μg mL^{-1} Primocin (Invivogen, cat# ant-pm-05), Glutamax (Thermo Fisher, cat# 35050061), and 10 mM HEPES (Thermo Fisher, cat# 12630080); L-WRN conditioned media was made using the L-WRN cell line (ATCC, cat# CRL-3276) as specified by the manufacturer's protocol and recommended reagents. Organoid density and size were monitored and passaged when criteria were met according to PDMR SOP40103. Organoid-BME domes were digested using 750 μg mL^{-1} Dispase II (Thermo Fisher, cat# 17105041).

Ganglia dissection for explants and dissociation

Mouse superior cervical ganglia (mSCG) were excised from neonatal mice 1–3 days post birth from wildtype C57Bl/6 mice. Mice were housed under controlled conditions with a regular light cycle with access to food and water *ad libitum* (IACUC Protocol TR02 IP00000674). SCGs were isolated following previously established protocols.[53] After dissection, isolated SCGs were washed in Dulbecco's modified Eagle's medium (DMEM) supplemented with 1% penicillin/streptomycin. For explant studies, ganglia were cut in two and used directly. For experiments involving dissociated neurons, the isolated ganglia were resuspended in 1 mL of type-2 collagenase (10 mg mL^{-1}) and incubated for 60 minutes at 37 °C in 5% CO_2 and relative humidity. The microcentrifuge tubes containing the ganglia were flicked and inverted every 15 minutes to help disrupt the ganglia. Isolated ganglia were then resuspended in complete neurobasal medium (neurobasal medium supplemented with 1× GlutaMAX (Gibco) + 1× B27 + 50 ng mL^{-1} 2.5S mouse nerve growth factor (NGF) (Gibco) + 1% penicillin/streptomycin) and dissociated by titration using a 5 mL Pasteur pipette.

Microgel loading on microfluidic devices

To load microgels into the chips, microgels were first centrifuged at 100 rcf for 20 s in microcentrifuge tubes. Excess PBS was removed, and the process was repeated. The devices were then exposed to corona treatment for 3 seconds. Five microliters of microgels were added to each chip, and the newly loaded chips were centrifuged at 100 rcf for 20 s. PBS or cell growth medium was then added to each media channel. For experiments containing dissociated neurons, 2×10^6 cells per mL were mixed with microgels prior to addition to the device.

Aspiration-assisted bioprinting into granular hydrogels

Particle placement was completed using the Sartorius CellCelector™ (Sartorius, Göttingen, Germany). The CellCelector™ includes a robotic arm with a replaceable capillary, a mobile stage with an inverted microscope, and a camera system to allow for visualization of the picking and dispensing process. Particles were first pipetted into a PDMS well for picking and placed onto the CellCelector™ stage along with a microgel-loaded chip. SCG explants and PC3 spheroids were picked using aspiration-assisted bioprinting to avoid fully aspirating and damaging the spheroid.[54–56] The capillary size was 1/5 to 1/4 of the spheroid diameter. An aspiration volume of 2 μL at 5% aspiration speed was used to move the particles.

Published on 15 aprile 2025. Downloaded on 06/02/2026 22:13:02.

Coculture conditions

For cocultures of mSCG neurons and PC3 spheroids, cells were cultured in 50 : 50 neurobasal : RPMI 1640 supplemented with 10% FBS + 1× GlutaMAX (Gibco) + 1× B27 + 50 ng mL^{-1} nerve growth factor (NGF) + 1% penicillin/streptomycin. mSCG neurons were cultured for one day on the chip before adding PC3 spheroids and then cocultured for 2 days. Cocultures of organoids were cultured in Organoid Basic Media and L-WRN conditioned media at a 1 : 1 ratio and supplemented with 1.25 mM *N*-acetylcysteine, 10 mM nicotinamide, B-27 supplement, N-2 supplement, 10 uM Y-27632, and 50 ng mL^{-1} NGF. Organoid-only controls were cultured in the same media as organoids cocultured with neurons. Organoid samples were cultured for 4 days. All samples were cultured under static conditions, with media replenished each day.

Microgel imaging

Fluorescence images of packed microgels were acquired on a CrestOptics X-Light V3 spinning disk confocal head (CrestOptics, Rome, Italy) with 50 um pinholes spaced 200 μm apart, attached to a Nikon TiE2 inverted microscope stand (Nikon USA, Melville, NY, USA). Laser-based excitation from a CELESTA VBCTGRN light engine (Lumencor, Beaverton, OR, USA) was combined with narrow bandwidth emission filters (Semrock, IDEX Health & Science LLC, West Henrietta, NY, USA) for fluorescence detection on a Kinetix back-illuminated sCMOS camera (Teledyne Photometrics, Tucson, AZ, USA). Stage movement in *xyz* and data acquisition were integrated under NIS Elements (Nikon USA, Melville, NY, USA). Brightfield images were acquired on an inverted EVOS microscope.

Live-cell imaging

Spheroids used to demonstrate spheroid packing on the chip were stained with the SPY650-FastAct™ kit for actin and the NucBlue™ Live Cell ReadyProbes™ Reagent (DAPI) kit. Samples were imaged on the spinning disk confocal microscope described above.

Immunofluorescence and imaging

Samples were washed with PBS, fixed for 15 minutes at room temperature using 10% formalin, and washed with PBS 3 times. Samples were permeabilized with 0.1% Triton-X/PBS for 30 minutes at room temperature and washed 3 times with PBS. Samples were blocked with 1.5% bovine serum albumin (BSA) for 30 minutes and washed 3 times with PBS. The primary antibodies Laminin Antibody (Invitrogen, PA1-16730) (1 : 100 dilution), KI-67 Recombinant Rabbit Monoclonal Antibody (SP6) (Invitrogen, #MA5-14520), CD31 Polyclonal Antibody (Invitrogen, #PA5-16301), or anti-neurofilament-M (Developmental Studies Hybridoma Bank, 2H3) were added to 0.15% BSA/0.01% Triton-X/PBS. Samples were sealed with parafilm, stored at 4 °C overnight, and then washed with PBS 3×. The secondary antibodies Alexa Fluor® 488 AffiniPure™ Alpaca Anti-Mouse IgG (615-545-214), Cy™3 AffiniPure™ Alpaca Anti-Mouse IgG (615-165-214), or Cy™5 AffiniPure™ Alpaca Anti-Rabbit IgG (H+L) (611-175-215) (Jackson ImmunoResearch) (1 : 250 dilution), were added to 0.15% BSA/0.01% Triton-X/PBS. For experiments with DAPI and actin staining, the ReadyProbes™ Reagent F-Actin Phalloidin Conjugates for actin and NucBlue™ Fixed Cell ReadyProbes™ Reagent (DAPI) kits, were added to the above solution following manufacturer protocols. Samples were sealed with parafilm, stored at 4 °C overnight, and then washed with PBS 3×. Samples were imaged the spinning disk confocal microscope described above. All images are *z*-stacks and are presented as *z*-projections using the maximum intensity method in Imaris. Acquisition settings were uniform across comparative experiments.

Histology and imaging

Samples were fixed with 4% paraformaldehyde (Thermo Scientific, cat#AAJ19943K2) for 45 minutes at room temperature and washed with 1× PBS three times. Hematoxylin was added for 5 minutes as a counterstain to visualize cell-dense regions and washed with 1× PBS. Samples were removed for downstream analysis by filling the open chamber of the device with hot 4% agarose, allowing the contents to cool and solidify, and carefully peeling the agarose-embedded sample block from the device. Agarose blocks were then processed for FFPE with a Tissue-Tek VIP 6 Vacuum Infiltration Tissue Processor through a series of graded ethanol washes (30 min 70% EtOH, 40 min 80% EtOH, 40 min 95% EtOH, 3× 40 min 100% EtOH), two 45 min xylene baths, and 3× 45 min paraffin infiltration steps. Processed samples were embedded in paraffin wax at a Tissue-Tek TEC6 embedding station (Sakura). Blocks were then cut into 5 μm-thick sections using a MICROM microtome (Thermo Scientific, HM 355S) and mounted on SuperFrost Plus (Fisherbrand cat#1255015) charged glass slides. Hematoxylin and eosin (H&E) staining was done as previously described.[57] Briefly, slides were baked at 60 °C for 30 minutes, washed in two changes of xylene for 5 minutes each, then rehydrated through graded ethanol washes (2 × 5′ 100% EtOH, 3′ 95% EtOH, 3′ 70% EtOH, ddH_2O). Rehydrated slides were incubated in Gill no. 2 hematoxylin (Sigma-Aldrich, cat#GHS232), bluing reagent (Dako Bluing Buffer, cat#CS702), and alcoholic eosin Y solution (Sigma-Aldrich, cat#HT110116). Stained slides were dehydrated through graded ethanol washes to xylene, then coverslipped with Epredia Cytoseal mountant (Fisher Scientific, cat#83104) prior to imaging. Histological sections were imaged with a Zeiss Axiocam 712 color camera attached to a 0.63× camera mount to a Zeiss Axio Observer 7 inverted microscope stand with a 20× lens.

Image processing and statistical analysis

Images were processed in the Imaris Image Analysis Software (v10.1.1), Nikon Elements Analysis Software (v6.02.03), or Fiji ImageJ.[58] The surface function in Imaris was used to render

 This journal is © The Royal Society of Chemistry 2025

Published on 15 aprile 2025. Downloaded on 06/02/2026 22:13:02.

organoids and spheroids. The FilamentTracer function in Imaris was used for neurite tracing. Measurements were obtained from 3-D images, and the maximum penetration depth was evaluated as the furthest any neurite within the spheroid was from the surface of the spheroid. All comparative images were acquired and processed equally. All statistics were performed in GraphPad Prism. Packing densities were analyzed with a two-way ANOVA and 1-sample *t*-tests ($p > 0.35$, $n = 3$). Explant and dissociated neuron studies were performed in duplicate. Studies of prostate cancer innervation were performed in triplicate. Comparisons of KI67 expression and the number of cells per organoid were made using 2-sample *t*-tests (Ki67 expression: $p < 0.0001$, $N = 1$, $n = 50$, df = 49; cells/organoid: $p = 0.0176$, $N = 1$, $n = 50$, df = 49). All data is presented as mean ± standard deviation.

Conclusions

Here, we presented an organ-on-a-chip platform that supports the development of engineered innervated granular hydrogel tissue constructs and the subsequent addition of organoids and spheroids. The device could support granular hydrogels made from a wide range of microgel materials ranging from 50–400 μm in diameter, with multiple geometries, and elastic moduli spanning multiple orders of magnitude. We next demonstrated that the device supports the growth and development of both mSCG whole explants and dissociated mSCG neurons. We demonstrated that the platform could innervate prostate cancer spheroids and patient-derived renal cell carcinoma organoids, and that innervation significantly increased the proliferation of renal cancer organoids. In summary, we present a versatile platform for innervating organoids with the capability to perform temporal organoid addition, build custom extracellular matrices, and remove the sample for downstream processing. This platform is an excellent option for targeting neurogenesis in tumours and will provide valuable insight into healthy and diseased function in organoids.

Data availability

Data for this article, including all raw images and raw data are available at Zenodo at **https://doi.org/10.5281/zenodo.15121190**, **https://doi.org/10.5281/zenodo.15122936**, and **https://doi.org/10.5281/zenodo.15122934**.

Author contributions

Conceptualization – J. F., D. M. R., G. T., S. E. E., and L. B. Data curation – J. F., D. M. R., and M. H. Formal analysis – J. F. and L. W. Funding acquisition – G. T., S. E. E., and L. B. Investigation – J. F., D. M. R, J. C., G. S., L. C., K. E., L. W., and M. H. Methodology – J. F., D. M. R, J. C., and L. B. Project administration – J. F., G. T., S. E. E., and L. B. Resources – G. T., S. E. E., and L. B. Supervision – G. T., S. E. E., and L. B. Validation – J. F., D. M. R., G. S., K. E., G. T., S. E. E., and L. B. Visualization – J. F., D. M. R., and M. H. Writing – original draft – J. F., D. M. R, J. C., L. C., and K. E. Writing – review & editing – J. F., D. M. R, J. C., G. S., L. C., K. E., L. W., G. T., S. E. E., and L. B.

Conflicts of interest

The authors have no conflicts of interest to declare.

Acknowledgements

This project was supported by funding from the following: National Institutes of Health grant R01DE029553, National Cancer Institute grants 5R01CA250378 and 1R21CA259440, Department of Defense grant W81XWH-15-9-0001, the Hope Foundation Award, and the OHSU Silver Family Innovation Award. Institutional support was provided by the Knight Cancer Institute and the Cancer Early Detection Advanced Research Center. We acknowledge expert technical assistance by staff in the Advanced Multiscale Microscopy Shared Resource, supported by the OHSU Knight Cancer Institute (NIH P30 CA069533) and the OHSU University Shared Resources Program. Equipment purchases included support from the OHSU Foundation, the Knight Cancer Institute, the MJ Murdock Charitable Trust, and the Collins Medical Trust. Device fabrication was supported by the Knight Cancer Institute Nanofab Facility. We would finally like to acknowledge Ariana Satler for graciously providing mSCG ganglia.

Notes and references

1 S. E. Honeycutt, P.-E. Y. N'Guetta and L. L. O'Brien, *Curr. Top. Dev. Biol.*, 2022, **148**, 195–235.
2 X. Li, X. Peng, S. Yang, S. Wei, Q. Fan, J. Liu, L. Yang and H. Li, *Cell Death Discovery*, 2022, **8**, 131.
3 H. Wang, Q. Zheng, Z. Lu, L. Wang, L. Ding, L. Xia, H. Zhang, M. Wang, Y. Chen and G. Li, *Cell Death Discovery*, 2021, **7**, 76.
4 D. Hanahan and M. Monje, *Cancer Cell*, 2023, **41**, 573–580.
5 S. Das, W. J. Gordián-Vélez, H. C. Ledebur, F. Mourkioti, P. Rompolas, H. I. Chen, M. D. Serruya and D. K. Cullen, *npj Regener. Med.*, 2020, **5**, 11.
6 M. Xia, J. Ma, M. Wu, L. Guo, Y. Chen, G.-L. Li, S. Sun, R. Chai, H. Li and W. Li, *Stem Cell Rep.*, 2023, **18**, 319–336.
7 P. Zhuang, A. X. Sun, J. An, C. K. Chua and S. Y. Chew, *Biomaterials*, 2018, **154**, 113–133.
8 A. Newman Frisch, L. Debbi, M. Shuhmaher, S. Guo and S. Levenberg, *Curr. Opin. Biotechnol.*, 2022, **73**, 188–197.
9 E. K. Sloan, S. J. Priceman, B. F. Cox, S. Yu, M. A. Pimentel, V. Tangkanangnukul, J. M. G. Arevalo, K. Morizono, B. D. W. Karanikolas, L. Wu, A. K. Sood and S. W. Cole, *Cancer Res.*, 2010, **70**, 7042–7052.
10 A. Barbieri, S. Bimonte, G. Palma, A. Luciano, D. Rea, A. Giudice, G. Scognamiglio, E. La Mantia, R. Franco, S. Perdonà, O. De Cobelli, M. Ferro, S. Zappavigna, P. Stiuso, M. Caraglia and C. Arra, *Int. J. Oncol.*, 2015, **47**, 527–534.

Published on 15 aprile 2025. Downloaded on 06/02/2026 22:13:02.

11 W. Qian, S. Lv, J. Li, K. Chen, Z. Jiang, L. Cheng, C. Zhou, B. Yan, J. Cao, Q. Ma and W. Duan, *Oncol. Rep.*, 2018, **40**, 3015–3023.
12 B. March, S. Faulkner, P. Jobling, A. Steigler, A. Blatt, J. Denham and H. Hondermarck, *Nat. Rev. Urol.*, 2020, **17**, 119–130.
13 S. M. Gysler and R. Drapkin, *J. Clin. Invest.*, 2021, **131**(11), DOI: **10.1172/jci147276**.
14 T. Takebe and J. M. Wells, *Science*, 2019, **364**, 956–959.
15 J. Kim, B.-K. Koo and J. A. Knoblich, *Nat. Rev. Mol. Cell Biol.*, 2020, **21**, 571–584.
16 M. Hofer and M. P. Lutolf, *Nat. Rev. Mater.*, 2021, **6**, 402–420.
17 Z. Zhao, X. Chen, A. M. Dowbaj, A. Sljukic, K. Bratlie, L. Lin, E. L. S. Fong, G. M. Balachander, Z. Chen, A. Soragni, M. Huch, Y. A. Zeng, Q. Wang and H. Yu, *Nat. Rev. Methods Primers*, 2022, **2**(94), DOI: **10.1038/s43586-022-00174-y**.
18 B. L. LeSavage, R. A. Suhar, N. Broguiere, M. P. Lutolf and S. C. Heilshorn, *Nat. Mater.*, 2022, **21**, 143–159.
19 V. Veninga and E. E. Voest, *Cancer Cell*, 2021, **39**, 1190–1201.
20 Y. Zhang, M. Liu, N. Xie, Z. Wang, C. Yu, J. Li and X. Zhou, *hLife*, 2024, DOI: **10.1016/j.hlife.2024.05.002**.
21 H. E. Besikcioglu, Ü. Yurteri, E. Munkhbaatar, L. Ye, F. Zhang, A. Moretti, C. Mota Reyes, C. Özoğul, H. Friess, G. O. Ceyhan, R. Istvanffy and I. E. Demir, *STAR Protoc.*, 2021, **2**, 100935.
22 E. Loffet, L. Brossard and M. M. Mahe, *Methods Cell Biol.*, 2020, **159**, 175–199.
23 L. A. Krattiger, D. B. Emiroglu, S. Pravato, L. O. Moser, O. A. Bachmann, S. Y. La Cioppa, G. J. R. Rivera, J. A. Burdick, A. J. deMello, M. W. Tibbitt and M. Ehrbar, *Adv. Funct. Mater.*, 2024, **34**, 2310507.
24 F. Della Sala, M. Biondi, D. Guarnieri, A. Borzacchiello, L. Ambrosio and L. Mayol, *J. Mech. Behav. Biomed. Mater.*, 2020, **110**, 103885.
25 J. P. Fredrikson, L. F. Domanico, S. L. Pratt, E. K. Loveday, M. P. Taylor and C. B. Chang, *Sci. Adv.*, 2024, **10**, eadk9185.
26 F. Millesi, S. Mero, L. Semmler, A. Rad, S. Stadlmayr, A. Borger, P. Supper, M. Haertinger, L. Ploszczanski, U. Windberger, T. Weiss, A. Naghilou and C. Radtke, *ACS Appl. Mater. Interfaces*, 2023, **15**, 12678–12695.
27 C. Song, P. Wang and H. A. Makse, *Nature*, 2008, **453**, 629–632.
28 L. Riley, G. Wei, Y. Bao, P. Cheng, K. L. Wilson, Y. Liu, Y. Gong and T. Segura, *Small*, 2023, **19**, e2303466.
29 A. L. Liu and A. J. García, *Ann. Biomed. Eng.*, 2016, **44**, 1946–1958.
30 A. E. Widener, S. Duraivel, T. E. Angelini and E. A. Phelps, *Adv. NanoBiomed Res.*, 2022, **2**, 2200030.
31 A. Lacroix, M. Hayert, V. Bosc and P. Menut, *J. Food Eng.*, 2022, **312**, 110738.
32 K. A. Kilian, B. Bugarija, B. T. Lahn and M. Mrksich, *Proc. Natl. Acad. Sci. U. S. A.*, 2010, **107**, 4872–4877.
33 J. Lee, A. A. Abdeen, K. L. Wycislo, T. M. Fan and K. A. Kilian, *Nat. Mater.*, 2016, **15**, 856–862.
34 M. A. Skylar-Scott, S. G. M. Uzel, L. L. Nam, J. H. Ahrens, R. L. Truby, S. Damaraju and J. A. Lewis, *Sci. Adv.*, 2019, **5**(9), DOI: **10.1126/sciadv.aaw2459**.
35 D. J. Shiwarski, A. R. Hudson, J. W. Tashman and A. W. Feinberg, *APL Bioeng.*, 2021, **5**, 010904.
36 T. J. Hinton, Q. Jallerat, R. N. Palchesko, J. H. Park, M. S. Grodzicki, H.-J. Shue, M. H. Ramadan, A. R. Hudson and A. W. Feinberg, *Sci. Adv.*, 2015, **1**, e1500758.
37 J. Yang, C.-C. Hsu, T.-T. Cao, H. Ye, J. Chen and Y.-Q. Li, *Neural Regener. Res.*, 2023, **18**, 657–663.
38 D. Jgamadze, J. Bergen, D. Stone, J.-H. Jang, D. V. Schaffer, E. Y. Isacoff and S. Pautot, *PLoS One*, 2012, **7**, e30293.
39 S. Pautot, C. Wyart and E. Y. Isacoff, *Nat. Methods*, 2008, **5**, 735–740.
40 S. E. Eksi, A. Chitsazan, Z. Sayar, G. V. Thomas, A. J. Fields, R. P. Kopp, P. T. Spellman and A. C. Adey, *Nat. Commun.*, 2021, **12**, 7292.
41 K. Ait-Ahmad, C. Ak, G. Thibault, Y. H. Chang and S. E. Eksi, *Heliyon*, 2025, **11**, e41209.
42 S. Dwivedi, M. Bautista, S. Shrestha, H. Elhasasna, T. Chaphekar, F. S. Vizeacoumar and A. Krishnan, *Cell Death Discovery*, 2021, **7**, 364.
43 A. H. Zahalka, A. Arnal-Estapé, M. Maryanovich, F. Nakahara, C. D. Cruz, L. W. S. Finley and P. S. Frenette, *Science*, 2017, **358**, 321–326.
44 M. Arese, F. Bussolino, M. Pergolizzi, L. Bizzozero and D. Pascal, *Ann. Transl. Med.*, 2018, **6**, 89.
45 M. Uhlen, C. Zhang, S. Lee, E. Sjöstedt, L. Fagerberg, G. Bidkhori, R. Benfeitas, M. Arif, Z. Liu, F. Edfors, K. Sanli, K. von Feilitzen, P. Oksvold, E. Lundberg, S. Hober, P. Nilsson, J. Mattsson, J. M. Schwenk, H. Brunnström, B. Glimelius, T. Sjöblom, P.-H. Edqvist, D. Djureinovic, P. Micke, C. Lindskog, A. Mardinoglu and F. Ponten, *Science*, 2017, **357**(6352), DOI: **10.1126/science.aan2507**.
46 R. D. Cervantes-Villagrana, D. Albores-García, A. R. Cervantes-Villagrana and S. J. García-Acevez, *Signal Transduction Targeted Ther.*, 2020, **5**, 99.
47 A. Takenaka, R. A. Leung, M. Fujisawa and A. K. Tewari, *World J. Urol.*, 2006, **24**, 136–143.
48 D. C. Duffy, J. C. McDonald, O. J. Schueller and G. M. Whitesides, *Anal. Chem.*, 1998, **70**, 4974–4984.
49 J. P. Fredrikson, P. P. Brahmachary, A. E. Erdoğan, Z. K. Archambault, J. N. Wilking, R. K. June and C. B. Chang, *Cells*, 2022, **11**, 900.
50 Z. Mahdieh, M. D. Cherne, J. P. Fredrikson, B. Sidar, H. S. Sanchez, C. B. Chang, D. Bimczok and J. N. Wilking, *Biomed. Mater.*, 2022, **17**(4), DOI: **10.1088/1748-605X/ac7306**.
51 X. Cui, Y. Hartanto and H. Zhang, *J. R. Soc. Interface*, 2017, **14**(127), DOI: **10.1098/rsif.2016.0877**.
52 D. Liu, S. Chen and M. Win Naing, *Biotechnol. Bioeng.*, 2021, **118**, 542–554.
53 M. Jackson and W. Tourtellotte, *Bio-Protoc.*, 2014, **4**(2), DOI: **10.21769/bioprotoc.1035**.
54 A. C. Daly, M. D. Davidson and J. A. Burdick, *Nat. Commun.*, 2021, **12**, 753.

 This journal is © The Royal Society of Chemistry 2025

55 B. Ayan, N. Celik, Z. Zhang, K. Zhou, M. H. Kim, D. Banerjee, Y. Wu, F. Costanzo and I. T. Ozbolat, *Commun. Phys.*, 2020, **3**, 1–14.
56 B. Ayan, D. N. Heo, Z. Zhang, M. Dey, A. Povilianskas, C. Drapaca and I. T. Ozbolat, *Sci. Adv.*, 2020, **6**, eaaw5111.
57 D. M. Roth, L. Puttagunta and D. Graf, *Methods Mol. Biol.*, 2022, **2403**, 187–200.
58 C. T. Rueden, J. Schindelin, M. C. Hiner, B. E. DeZonia, A. E. Walter, E. T. Arena and K. W. Eliceiri, *BMC Bioinf.*, 2017, **18**, 529.

Published on 15 aprile 2025. Downloaded on 06/02/2026 22:13:02.